Low order physical models of vertical axis wind turbines

Cite as: J. Renewable Sustainable Energy **9**, 013306 (2017); https://doi.org/10.1063/1.4976983
Submitted: 12 September 2016 . Accepted: 03 February 2017 . Published Online: 28 February 2017

Anna E. Craig, John O. Dabiri, and Jeffrey R. Koseff

Low order physical models of vertical axis wind turbines

Anna E. Craig,[1,a)] John O. Dabiri,[2] and Jeffrey R. Koseff[3]
[1]*Department of Mechanical Engineering, Stanford University, Stanford, California 94035, USA*
[2]*Department of Civil and Environmental Engineering, Stanford University, Stanford, California 94035, USA and Department of Mechanical Engineering, Stanford University, Stanford, California 94035, USA*
[3]*Department of Civil and Environmental Engineering, Stanford University, Stanford, California 94035, USA*

(Received 12 September 2016; accepted 3 February 2017; published online 28 February 2017)

In order to examine the ability of low-order physical models of vertical axis wind turbines to accurately reproduce key flow characteristics, experimental data are presented for the mean flow patterns and turbulence spectra associated with pairs of rotating turbines, rotating solid cylinders, and stationary porous flat plates (of both uniform and non-uniform porosities). The experiments were conducted at a nominal model-diameter Reynolds number of 600 and rotation tip speed ratios between 0 and 6. By comparing the induced flow fields of the different models both qualitatively and quantitatively, it was concluded that the two dimensional horizontal mean flow fields induced by the porous flat plates were quantitatively similar to those induced by slowly rotating turbine models. However, over the range of the experimental parameters examined, the porous flat plates were unable to produce vertical flows similar to those associated with the slowly rotating turbine models. Conversely, the moderately rotating cylinders induced three dimensional mean flow fields quantitatively similar to those induced by rapidly rotating turbine models. These findings have implications for both laboratory experiments and numerical simulations, which have previously used analogous low order models in order to reduce experimental/computational costs. Specifically, over the range of parameters examined, the comparison between induced flow fields of the different model fidelities allows identification of the lowest cost model for which the specific goals of a study can be obtained, to within the desired accuracy. And if a lower fidelity model is used, it is possible to incorporate into the analysis of the collected data an understanding of how the results would be expected to vary from a higher fidelity case. *Published by AIP Publishing*. [http://dx.doi.org/10.1063/1.4976983]

I. INTRODUCTION

In recent years, vertical axis wind turbine (VAWT) arrays have attracted significant attention as a potentially valuable and versatile approach to wind energy extraction.[1–8] Of particular interest has been the spatial and rotational configuration of the turbines in these arrays, which determines the nature of the interaction between the turbines and thus the overall power output of the array.

Field experiments[1,4,5] provide the most direct method for testing different array configurations but have the disadvantage of typically involving only small numbers of turbines and being expensive and time-consuming to conduct, thus limiting the number of configurations which can be tested. Furthermore, measurements beyond the power output of the array or single point velocity measurements are difficult to obtain, which inhibits our ability to understand the underlying dynamic interactions among the turbines.

[a)]Email: craig0a@stanford.edu

Numerical simulations alleviate many of these difficulties, providing a controlled set of conditions under which to test a given array and the ability to collect 3 velocity component, high-resolution, high-frequency flow measurements throughout the entire simulation domain. The tradeoff is the computational time and cost, which to date have restricted large-array simulations to either 2D Unsteady Reynolds Averaged Navier Stokes (URANS) simulations[3,9] or 3D Large Eddy Simulations (LESs).[2,10] Although the 2D simulations have typically modeled the turbine geometry to high fidelity, they require an underlying assumption that the horizontal plane interactions between turbines in the array are sufficient to understand the performance of the arrays, without any contribution or influence from interactions with the freestream flow above the array or the bottom boundary layer. This assumption is called into question by the results of both field work[4,5] and laboratory experimental work,[7,8] which indicate the importance of the three-dimensional interactions, particularly through the top of the array. Underlying the 3D LES simulations are assumptions concerning the modeling of the turbine: as an actuator line model (or immersed boundary model), an actuator swept surface model, or an actuator "disk" (flat plate) model. Some LES work has been done validating the LES immersed boundary model against laboratory experiments for a single VAWT[11,12] and some direct numerical simulation (DNS) work has been conducted to elucidate the impact of selecting one LES model over the other, again in the case of a single VAWT.[13,14] In particular, an actuator line model, in which each blade was represented by a moving line of point forces, has been compared to an actuator swept-surface model, in which the time-averaged forcing of the blades was distributed over the cylindrical surface swept out by the blades.[14] It was shown that the actuator line model was better able to capture the unsteady nature of the wake and, in particular, showed faster wake recovery as a result of better modeling of the wake turbulence intensity. However, the actuator swept-surface model captured mean flow characteristics and was the lower-computational cost model. An even lower computation cost model is the actuator disk model, which represents the drag force exerted by a turbine (horizontal or vertical axis) on the flow in the streamwise direction over the projected frontal area of the turbine. Although the distribution of the drag forcing over the disk may be non-uniform in order to introduce downstream asymmetries in the wake, in general any rotationally induced flow behaviors cannot be represented.[15–19]

Laboratory experiments also alleviate some of the difficulties associated with field experiments. Similar to the numerical studies, they provide a controlled test environment, relatively easy reconfiguration of the arrays, and reasonable spatial coverage of (at least) 2 velocity component flow measurements. In the laboratory experiments reported to date,[7,8] however, multiple simplifications to the physical array were required in order to test the large arrays desired. These simplifications included reduced Reynolds number, externally driven elements (at a constant rotation rate throughout the array), and modeling the turbines as cylinders. A full discussion of the implications of the simplifications was given in the supplementary materials of Craig *et al.*,[7] from which it was concluded that while there were some strong similarities between the examined rotating cylinder arrays and VAWTs, additional work needed to be undertaken to further characterize similarities and differences. One key question identified was to what extent the increase in solidity of the array elements from the bladed turbine to a solid cylinder would influence the flow kinematics.

The present work seeks to examine this open question by experimentally comparing the 3D flow patterns around pairs of either scaled VAWT models or solid cylinders (hereafter collectively referred to as "elements"). The implications of this study, however, are not limited to further understanding the level of analogy between the previously reported experiments and a physical VAWT array. Because the experimental modeling of turbines as solid cylinders corresponds closely to numerical modeling of the turbines as actuator swept surfaces, this study is also helpful in understanding how useful numerical studies are in characterizing the quality of the analogy. Taking this application of the present work a step further, pairs of mesh plates with the same projected frontal area as the turbines were also tested as the physical analog of the actuator disk models from numerical simulations.[15–19]

The goal of the present work is therefore to characterize the similarities and differences in the mean and turbulent flow patterns induced by elements of different geometries (turbine,

cylinder, and porous flat plate) operating over a range of rotation rates (where appropriate). This characterization is intended to be used as a framework, allowing the viability of low-order VAWT models to be evaluated for a given study, taking into consideration both the operating conditions of the VAWT array to be modeled and the intended purpose of the study.

The remainder of this work will be organized as follows: Section II will give a description of the experimental setup. Section III will present the results, focusing first in Section III A on the time averaged flow patterns and integral mean momentum fluxes associated with the cylinder, turbine, and mesh elements and in Section III B on the wake turbulence spectra of the cylinder and turbine models. Section IV discusses these results and the implications for experimental and numerical modeling of VAWTs.

II. EXPERIMENTAL METHODS

A. Notation

The non-dimensional rotation rate is defined to be $\alpha = D\Omega/2u_0$, where D is the element diameter, Ω is the rotational speed of the element, and u_0 is the freestream velocity. The pertinent Reynolds number is defined by the element diameter and freestream velocity, that is $Re = u_0 D/\nu$, where ν is the kinematic viscosity of the working fluid.

B. Facilities

Experiments were conducted in the recirculating water flume of the Bob and Norma Street Environmental Fluid Mechanics Laboratory at Stanford University. The coordinate system used in this work took the positive x direction to be aligned with the freestream flow and the z direction to be vertically upwards, leaving the y direction aligned transversely across the flume. As shown in Figure 1(a), the coordinate system origin was taken to be between the two elements in the pair (i.e., along the transverse centerline of the elements and at the line of transverse symmetry) and at the bottom of the elements.

Two-dimensional particle image velocimetry (PIV) was used to collect data in both vertical (x–z) planes and horizontal (x–y) planes, as shown in Figure 1(b). The horizontal data were collected at $z = 4.0D$, $5.4D$, and $7.5D$. The vertical sheet data were collected at $y = 0.0D$, $-1.0D$,

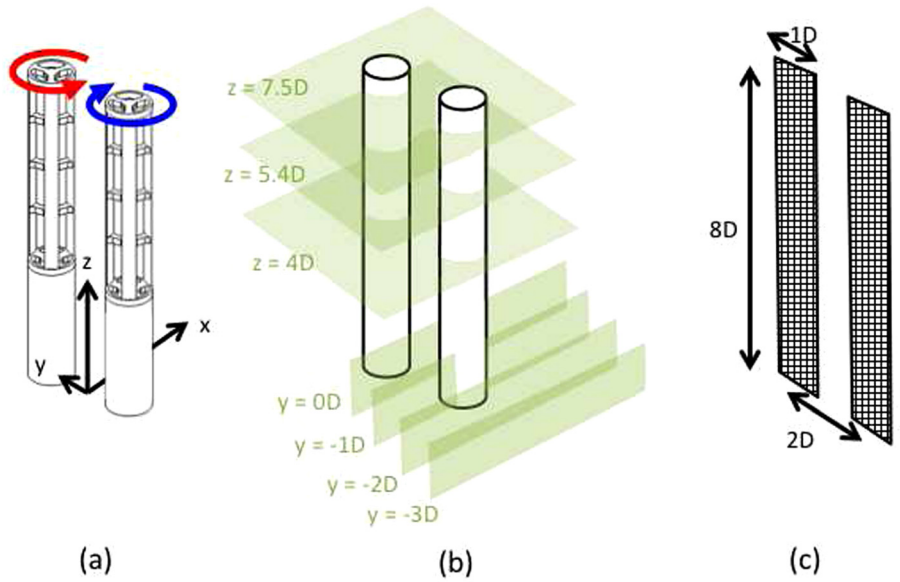

FIG. 1. Schematics of experimental configurations and parameters. (a) Turbine models shown with origin and orientation of coordinate system and rotational sense of the elements. (b) Cylinder models shown with locations of vertical and horizontal PIV data sheets (note: sketch does not represent the full field of view for each sheet). (c) Mesh models shown with dimensions of elements and center-to-center spacing of elements.

$-2.0D$, and $-3.0D$. Details of the data collection and processing may be found in the supplementary materials.

The majority of the vertical sheet data at $y = 0.0D$ and $y = -1.0D$ and the data on the mesh elements were collected in a separate setup of the experiment than the vertical sheet data at $y = -2.0D$ and $y = -3.0D$ and all horizontal sheet data for the cylinder and turbine elements. The two installments had different freestream velocities: 4.70 ± 0.02 cm/s and 5.00 ± 0.02 cm/s, resulting in Reynolds numbers of 597 ± 3 and 635 ± 3, respectively. All reported velocities are normalized by the (appropriate) freestream velocity, u_0. The variation in the (appropriately normalized) mean flows between analogous data sets collected in the two installments was, with minor exceptions, within experimental uncertainties, indicating that the variation in flows caused by the difference in Re was minor or negligible.

It is noted that the present set of experiments was conducted at Reynolds numbers several orders of magnitude lower than that of most commercial wind turbines ($Re \sim O(10^2)$ versus $Re \sim O(10^5$–$10^6)$). Given the similar nature of turbulent flows, however, it is argued that if the flow was fully turbulent through both ranges of Re, the (lower order) flow statistics should be considered to be similar between the experiments and the physical array.[20] In order to determine if the flow was turbulent, vertical sheets of data were taken with elements removed (i.e., the empty flume boundary layer). Averaging over the full streamwise width of the measurement volume, the momentum thickness Reynolds number ($\theta = \int_0^\infty \frac{u}{u_0}(1 - \frac{u}{u_0})dz$, $Re_\theta = \frac{\theta u_0}{\nu}$) was computed to be 306. It has previously been argued that this momentum thickness Reynolds number is sufficient to establish a turbulent boundary layer, albeit the turbulence may be "sustained" rather than "fully developed."[21]

More directly, the data were compared to the classical multi-layer law of the wall model for turbulent boundary layer flows over smooth walls (details provided in supplementary materials.) Although comparison is made to the smooth wall boundary layer, it is noted that the present flow was perturbed from this classical case by the sparse roughness of the element mounting point protrusions (roughness Reynolds number of 26, not much greater than for a smooth plate) and holes associated with the top plate of the experimental setup. Therefore exact agreement would not be expected. For the present discussion, it is most important to note that the data showed agreement with the log region model over $z^+ \in [30, 150]$, given an appropriately matched u_τ (friction velocity), as shown in Figure 2. This may be taken as indication that the flow was fully turbulent.[21] It is noted that at higher values of z^+, the present flow field showed the opposite deviation from the log law than the classically observed wake;[22,23] this feature of the flow is believed to be associated with the specific design of the downstream weir in the flume.

As a final point of comparison, for the same basic experimental setup and similar flume flow speed, but with a large array of cylinder elements, data was collected over a range of Reynolds numbers: $Re = 600$, 1200, and 2400.[7] Comparing the data taken at the leading edge of the array (for various element rotation rates) the mean vertical, streamwise, and Reynolds

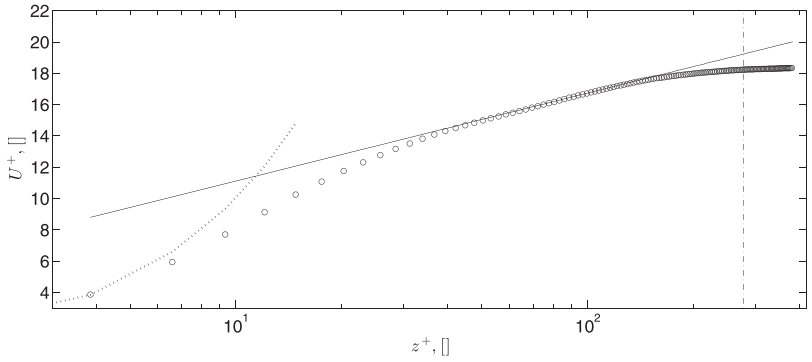

FIG. 2. Comparison of data to law of the wall model. The open circles indicate the data, the dotted line indicates the viscous sublayer model, the solid line indicates the log layer model, and the vertical dashed-dotted line indicates the height of the elements.

stress flow profiles were similar across Reynolds numbers, as shown in Figure 3. Again, this may be taken as indication that all three Reynolds numbers were within a similar turbulent flow regime.

C. Models

All elements were 12.7 mm in diameter (or width in the case of the meshes) (D) and the overall height of each element was 101.6 mm ($8D$), as shown in Figure 1(c). Pairs of elements had a transverse center-to-center spacing of 25.4 mm ($2D$).

The turbine elements (shown in Figure 4) were composed of two parts: a rotor formed by additive manufacturing which was mounted on a solid cylinder tower (both of diameter 12.7 mm). The height-diameter aspect ratio of the rotor was selected to equal with that of the Windspire turbine 5.08; therefore the height of the rotor was 64.6 mm and the height of the cylinder tower was 37.0 mm. The model had three NACA 0018 blades of chord length (c) equal to 1/3 of the diameter (4.23 mm). This resulted in a turbine solidity ($\sigma = \frac{nc}{\pi D}$, where n is the number of blades[24]) of 0.32. One turbine was manufactured with the blades oriented for clockwise rotation (when viewed from above) and one turbine was manufactured with the blades oriented for counter clockwise rotation (also when viewed from above).

The porous plate elements were constructed of a stainless steel mesh with an overall solidity of 0.39 (i.e., 61% porosity, 12×12 mesh with wire diameter of 0.46 mm and opening size of 1.7 mm). By layering the mesh with shifts between the meshes of the layers, different solidities and solidity gradations could be achieved. For example, if two layers were closely aligned the solidity remained roughly 0.39, whereas if the openings of two layers were shifted 50% vertically and 50% horizontally with respect to each other, the resulting solidity was roughly 0.70. This is illustrated in Figure 5, which features sketches of the models and estimates of the

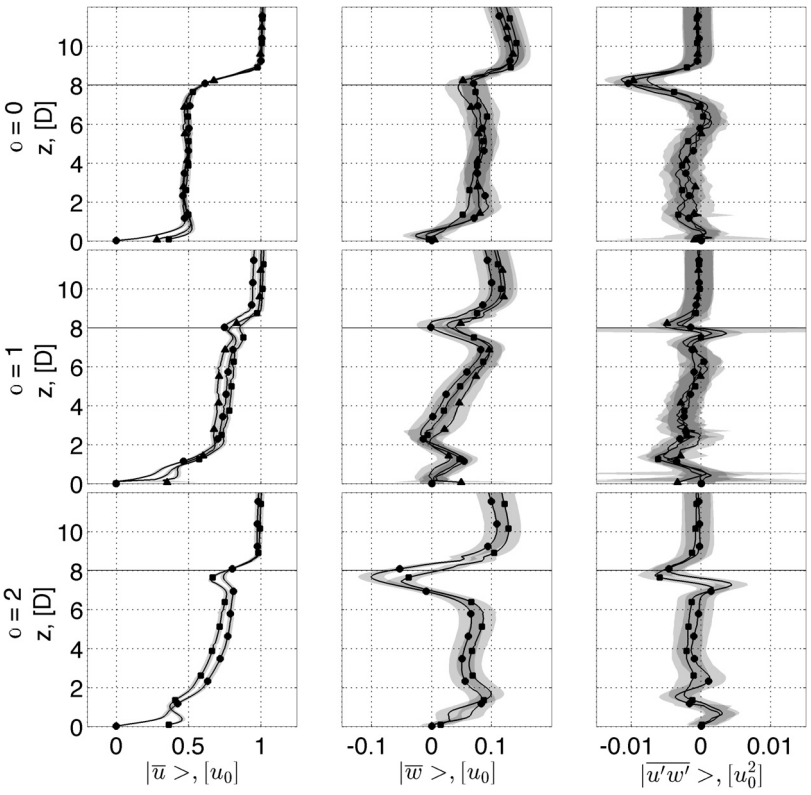

FIG. 3. Comparison of partially spatially averaged flow profiles for increasing Reynolds numbers at the leading edge of a large array of cylindrical elements. ○ indicates $Re = 600$, □ indicates $Re = 1200$, and △ indicates $Re = 2400$. Shaded regions indicate bootstrapped 95% confidence interval summed with propagated experimental uncertainties.

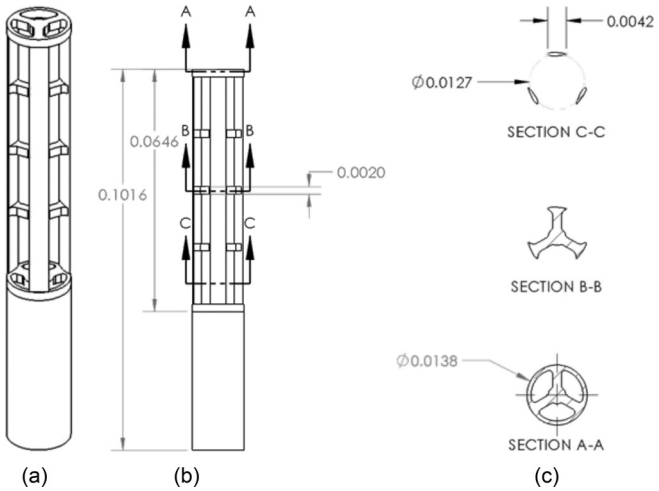

FIG. 4. Left: Isometric view of the printed turbine mounted on the cylinder "tower." Middle: side view of the model, showing vertical dimensions and locations of cross-sections. Right: cross-sectional views of the model: section A-A is the top ring/internal support, section B-B is one of the internal supports, section C-C is the blades. Dimensions are in m.

average solidities. Two duplicates of each model were fabricated and placed in the side-by-side configuration of the cylinder and turbine pairs, as shown in Figure 1. The model configurations and measurement planes are given in Table I.

D. Element rotation

The rotation of the elements in the work reported here was such that the inner edges of the pair moved downstream as shown in Figure 1(a). The opposite rotational sense, in which the

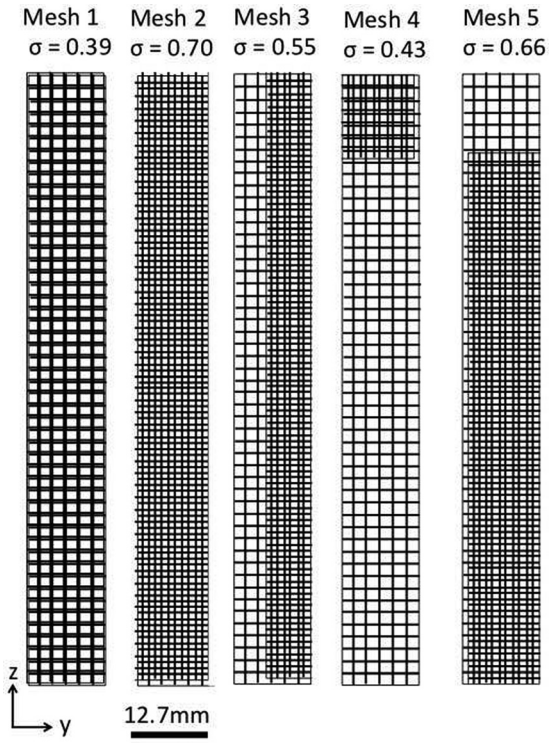

FIG. 5. Sketches of tested meshes as they would be seen from the y-z plane; their extent in the streamwise direction would only be that of one or two layers of mesh.

TABLE I. Summary of tested mesh configurations and data planes collected for each configuration.

Mesh/test reference	Configuration	Data planes collected
Mesh 1	Aligned perpendicular to flow	Horizontal, vertical
Mesh 2a	Aligned perpendicular to flow	Horizontal, vertical
Mesh 2b	Angled inward	Horizontal
Mesh 2c	Angled outward	Horizontal
Mesh 3a	Denser mesh at inner edges of pair	Horizontal
Mesh 3b	Denser mesh at outer edges of pair	Horizontal
Mesh 4	Aligned perpendicular to flow	Vertical
Mesh 5	Aligned perpendicular to flow	Vertical

inner edges of the pair moved upstream, was also examined, but for the sake of brevity and since the same conclusions may be drawn from both sets of data, the data and analysis associated with that rotational configuration are not reported here.

Element rotation was accomplished by creating chains of spur gears, sandwiched in place between a bottom and top plate, as shown in Figure 6. (A more complete description may be found in Craig *et al.*[7]) Two of the spur gears were fitted with shafts that protruded through the top plate and provided a mounting point for the elements above the top plate. The cylinder and turbine elements could be screwed onto these protruding shafts, while mounting clay was used to affix the meshes to these points.

Offset roughly 0.2 m transversely and 0.6 m downstream of the element pair, the last spur gear in the chain was fitted with a very long shaft which also protruded through the top plate and was connected to a DC motor above the array. The voltage supplied to the motor controlled

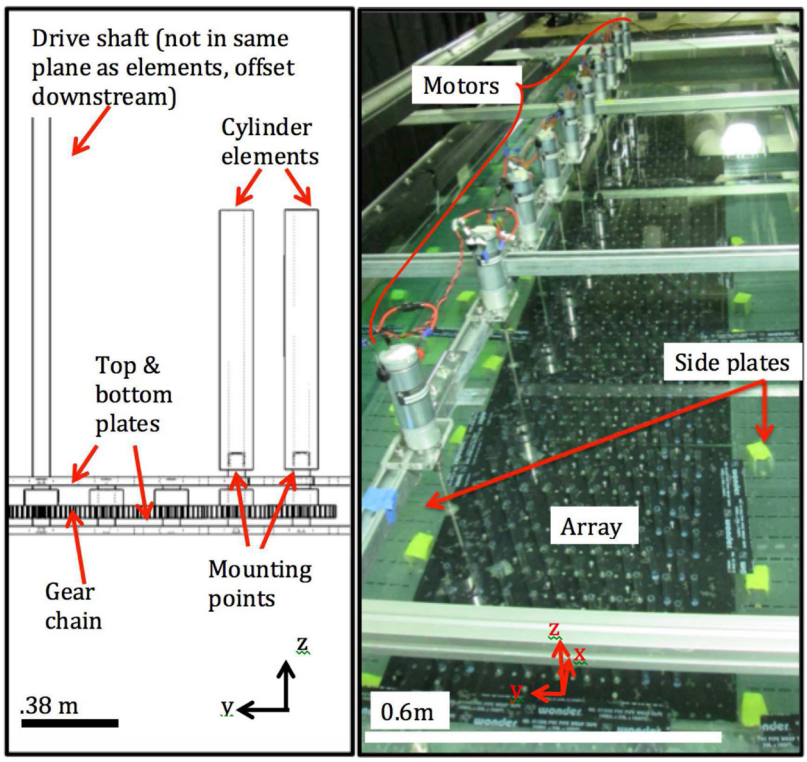

FIG. 6. Left panel: schematic of gear chain and element mounting scheme. Right panel: setup within flume; in this case only one motor and one section of the array were used, as opposed to the full array setup pictured. Adapted from Refs. 7 and 8.

the rotation rate of the gear chain and therefore of the elements. Data was collected with the cylindrical elements driven to (nominal) tip speed ratios of $\alpha = [0, 2, 4]$ and the turbine elements driven to (nominal) tips speed ratios of $\alpha = [0, 1, 2, 4, 6]$. The achieved tip speed ratios were $[0.99 \pm 0.08,\ 1.99 \pm 0.11,\ 3.99 \pm 0.18,\ 6.00 \pm 0.26]$ for the first experimental installment and $[0.93 \pm 0.08,\ 1.88 \pm 0.10,\ 3.75 \pm 0.16,\ 5.64 \pm 0.24]$ for the second experimental installment. For convenience, all cases will be referred to by the nominal values.

As the spur gear sandwich had a finite thickness, additional raised plates were used to fill the flume in front, in back, and to the sides of the setup so that a consistent offset bottom was formed, as shown in Figure 6. The most upstream plate was angled so as to provide a ramp up to the offset bottom and also provide a trip for the boundary layer.

III. RESULTS

A. Induced mean velocities

In order to qualitatively understand the mean flows induced by the different element geometries, contour plots of $\bar{u}, \bar{v}$ in the $z = 5.4D$ measurement plane and of $\bar{u}, \bar{w}$ in the $y = -1D$ measurement plane are compared in Figures 7 and 9, respectively. In the horizontal plane data, please note that only half of the measurement field is shown in order to simplify the data presentation: across the centerline $y = 0D$, $\bar{u}$ was effectively symmetric while $\bar{v}$ was effectively anti-symmetric. In the figures, the horizontal data for Mesh 1 and Mesh 2a are omitted for brevity, as these meshes exhibited symmetric wakes which were less comparable to the wakes induced by the higher fidelity turbine models.

In the horizontal plane, the mean flow patterns in streamwise velocity (Figure 7(a)) around the turbine models (middle column) showed three defining features: a region of significantly accelerated flow between the turbines (a); a decelerated flow wake region (b); and, for the higher rotation rates, a region of reversed flow near the upstream moving edge of the turbine (c). Comparing the turbines across rotation rate, with increasing α the wakes appear to have recovered more rapidly in the streamwise direction and are also increasingly angled away from the centerline with downstream distance. The three characteristic flow features were reproduced by the cylinder geometry, with some notable differences. The mesh geometries were able to reproduce the wake region (b) and Mesh 2c was even able to form a recirculation region (c). As the behavior of the turbines appears to have followed a progression over α, it is noted that the flow patterns associated with the meshes tended to resemble the lower α turbine flow patterns while the flow patterns associated with the cylinders tended to resemble the higher α turbine flow patterns.

The mean flow patterns as shown by the transverse velocity fields (Figure 7(b)) around the turbine models (middle column) showed five distinguishing features: convergent flow (across the centerline) upstream over some capture region between the turbines (d), divergent flow (across the centerline) around the upstream outer edges of the turbine pair (e), and a strong divergent flow concentrated on the trailing edge of the turbine (f), but extending into the downstream region (g), with the exception of a region pulling flow into the wake (h). Comparing the turbines across rotation rate, with increasing α region (h) tended to spatially shift upstream so that it was closer to the turbine and also became spatially smaller. The cylinder at $\alpha = 2$ showed agreement with these key flow features, especially those associated with the higher α. The cylinder at $\alpha = 4$ largely produced the same flow patterns, but there was no wake pull-in region (h). The lack of a pull-in region h in this case may be due to a shift in the underlying wake vortex shedding behavior, which will be discussed in the quantitative context of Section III B. However, here it is noted that there is also some qualitative suggestion of a different wake behavior in the corresponding streamwise flow, shown in Figure 7(a). Here it is seen that the streamwise flow magnitude along a line connecting the outer edge of the cylinder pair to the far downstream wake is not monotonically growing; there is a local maximum of streamwise flow magnitude between the flow reversal region and the far downstream wake region, which is not seen in any other case. The meshes appear to have successfully captured the convergence and divergence ((d) and (e), respectively) upstream of the element and also showed the wake

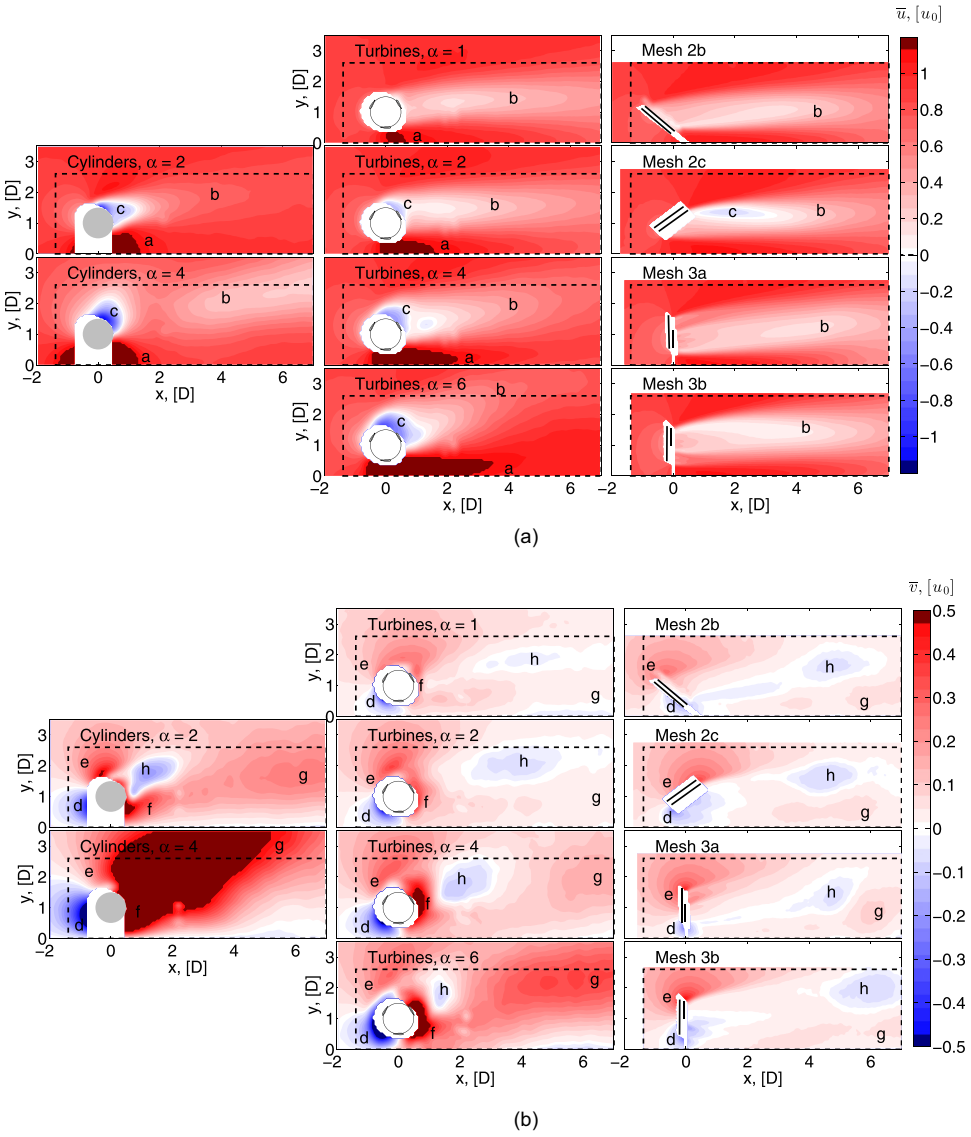

FIG. 7. Time averaged (a) $\bar{u}$ and (b) $\bar{v}$ in the horizontal measurement plane at $z = 5.4D$. The shown cylinder and turbine elements are counter-clockwise rotating (as viewed from above.) The thin dash-dot line indicates the region for which no data was available due to laser shadowing or element blockage. The dashed rectangle indicates the boundaries of the integral mean momentum flux control surface. Annotated features: a, accelerated streamwise flow between elements; b, reduced streamwise flow (wake) behind elements; c, reversed streamwise flow behind/to outer edge of elements; d, upstream transverse convergent flow between paired elements; e, upstream transverse divergent flow around paired elements; f, transverse divergent flow in near wake; g, transverse divergent flow in far wake; and h, transverse pull-in flow to wake.

pull-in zone (h), albeit very far downstream from the element, thus bearing the most similarity to the slowest rotating turbines. The meshes also captured the far downstream divergence behavior (g), but lacked the near-element divergence (f). This latter result is not surprising as the near-wake divergence is likely directly associated with the rotation of the element, which is absent in the case of the stationary meshes.

In order to compare the different models in a more quantitative way, the integral streamwise and transverse mean momentum fluxes ($J_x = \oint_{\partial V} \rho(\vec{\bar{u}} \cdot \hat{n})\bar{u}\, dA$ and $J_y = \oint_{\partial V} \rho(\vec{\bar{u}} \cdot \hat{n})\bar{v}\, dA$, respectively) were computed through the rectangular control surfaces shown by the dashed lines in Figure 7 and compared across the different element geometries and rotation rates. The extent of the control volume was chosen to be the maximum possible such that the same control volume could be considered across all cases. It would be of interest in future work to evaluate the

relative spatial decay rates of the mean flows induced by the different models, by considering multiple control volumes encompassing increasingly large spatial regions. In order to parameterize the geometry/rotation rate of a given test configuration, the dynamic solidity of the elements (σ_D) as defined by Araya *et al.*[24] is adopted

$$\sigma_D = 1 - \frac{1}{2\pi\sigma\alpha},$$

where σ represents the geometric solidity of the element and again, α is the non-dimensional rotation rate of the element ($\alpha = D\Omega/2u_0$, where D is the element diameter, Ω is the rotational speed of the element, and u_0 is the freestream velocity). It is noted that the definition of dynamic solidity was developed in the context of rotating turbines and stationary cylinders. The physical meaning of the expression for a rotating cylinder is not necessarily clear, as with any non-infinite rotation rate the dynamic solidity is lower than the geometric solidity of 1. Nevertheless, this parameterization provides a useful starting point in quantifying the different regimes of qualitatively observed behaviors.

As shown in Figure 8, J_x as induced by meshes 3b, 2b, and 2c ($\sigma_D = [0.55, 0.70, 0.70]$, respectively) were within the range of J_x as induced by slower rotating turbines ($\alpha = [1, 2]$, $\sigma_D = [0.5, 0.75]$). Furthermore, J_y as induced by meshes 3a and 3b ($\sigma_D = 0.55$) were also within the range of

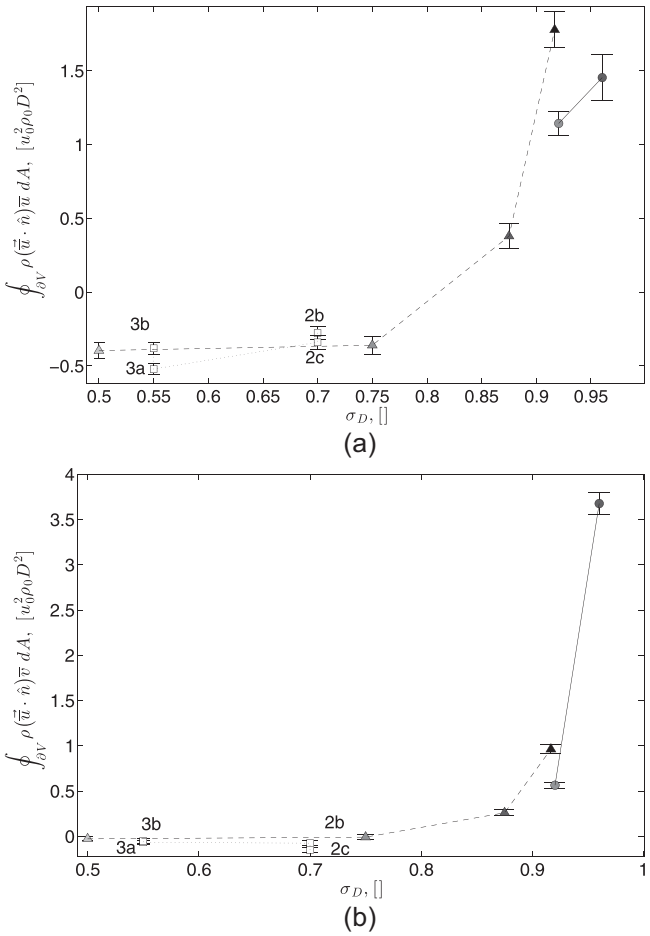

FIG. 8. (a) Streamwise and (b) transverse momentum fluxes through control volumes shown as dashed rectangles in Fig. 7. □ indicates a mesh element, △ indicates a turbine element, and ○ indicates a cylinder element. Greyscale indicates rotation rate, with white being stationary and black being $\alpha = 6$. Annotation is used to distinguish the different meshes. Error bars indicate the bootstrapped 95% confidence interval summed with the propagated experimental uncertainties. The lines simply connect the data points for each element type and do not represent a fitting to the data.

J_y induced by the slower rotating turbines. Therefore, mesh 3 may be considered to induce mean flows representative of those induced by turbines operating within the range $\sigma_D \in [0.5, 0.75]$. Similarly, J_x and J_y as induced by the moderately rotating cylinders ($\alpha = 2$, $\sigma_D = 0.92$) fell into the range of J_x and J_y as induced by the rapidly rotating turbines ($\alpha = [4, 6]$, $\sigma_D = [0.88, 0.92]$). Therefore, a moderately rotating cylinder may be considered to induce mean flows representative of those induced by rapidly rotating turbines. It is also noted that J_x and J_y followed the trend of increasing with increasing dynamic solidity, for both the turbine and cylinder geometries.

In the vertical plane passing through an element, the mean streamwise velocity (Figure 9(a)) associated with the turbines showed four characteristic features: at sufficiently high α there was a region of accelerated flow just above the end of the element (A) which increases in strength/magnitude with increasing α; there was a wake region, including some regions of upstream flow, primarily over the vertical region behind the turbine rotor (B); at sufficiently high α the wake region (B) was reduced in streamwise extent and was accompanied by a region of reduced flow which appears to originate near the top trailing edge of the turbine and which extends downwards with increasing streamwise distance (C); and finally, originating near the bottom trailing edge of the turbine and extending upwards with increasing streamwise distance, there was a region of upstream flow (D). The cylinder elements most closely reproduced the flow fields associated with the faster rotating turbines, clearly showing regions (A), (C), and (D) but showing only marginal wake regions (B). Referring back to the streamwise flows as measured in the horizontal planes, this corresponds to the stronger wake suppression behaviors associated with the cylinder elements in comparison to the turbine elements. In contrast, the meshes most closely resembled the slower rotating turbines, primarily showing regions (A), (B), and (D), but largely failing to reproduce region (C). Based on the full complement of data, the authors speculate that flow region (C) is associated in the case of the rotating elements with induced vortical structures, similar in nature to those detailed by Sumner[25] for stationary cylinder elements. However, as the data set collected was not well suited to educing the turbulence

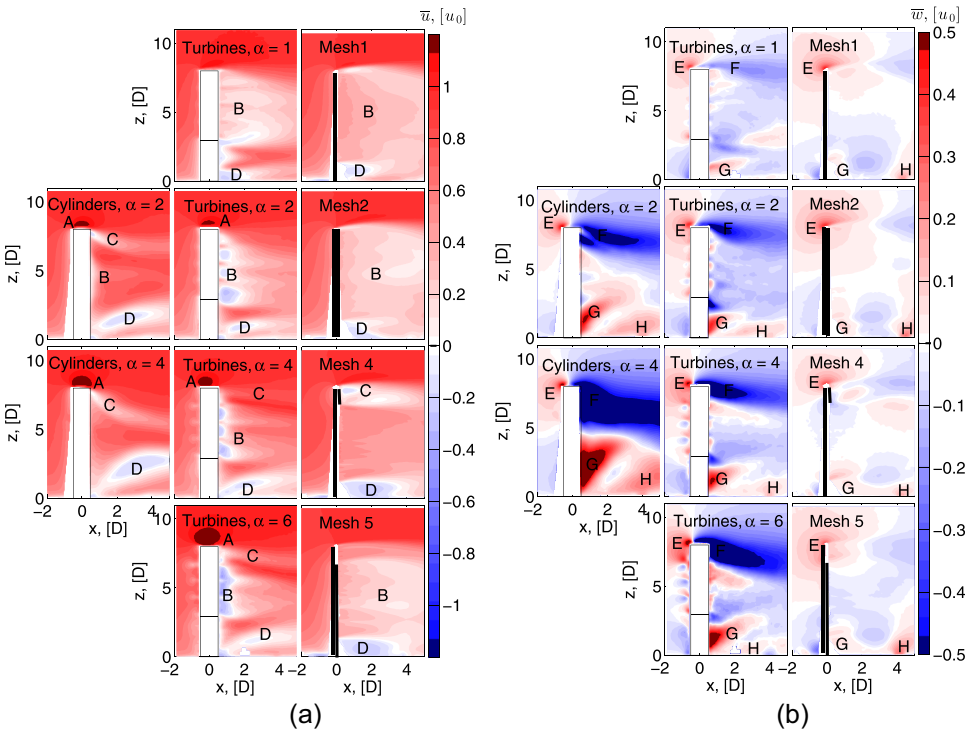

FIG. 9. Time averaged (a) $\bar{u}$ and (b) $\bar{w}$ in the vertical measurement plane at $y = -1D$. Annotated features: A, accelerated streamwise flow acceleration over element top; B, reduced streamwise flow (wake) behind element; C, reduced streamwise flow behind element top trailing edge; D, reversed streamwise flow behind element bottom trailing edge; E, upward flow in front of element top leading edge; F, downward flow behind element top trailing edge; G, upward flow near element bottom trailing edge; and H, upward flow near bottom in downstream of element.

structures of the flow, this remains simply a speculation and the underlying physical mechanisms explaining the presence of region (C) for the turbine and cylinder models and the lack of a clear region (C) for the mesh models is left open for future research.

Finally, the mean vertical flows (Figure 9(b)) associated with the turbines showed four basic flow regions: a region of positive flow over the top leading edge of the element (E); a region of negative flow behind the top trailing edge of the element (F); and two regions of positive flow near the bottom boundary—one very close to trailing edge of the element (G) and one further downstream (H). Comparing the turbines across rotation rate, with increasing α the strengths of regions (E), (F), and (G) all increased while region (F) angled more sharply downward over streamwise distance and region (G) angled more sharply upward over streamwise distance. The cylinders very closely reproduced the same flow regions, especially in comparison with the higher turbine rotation rates. The meshes reproduced regions (E), (G), and (H), but it was not clear that they reproduced the downward flow (F) behind the cylinder. There were regions spatially further downstream which might be considered analogous but have not been considered so here, as they were not clearly associated with the top trailing edges of the elements. Again, determining the precise physical mechanisms for this difference remains open to future work.

Figure 10 presents the more quantitative metric of integral streamwise and vertical mean momentum fluxes ($J_x = \oint_{\partial V} \rho(\vec{u} \cdot \hat{n})\bar{u}\, dA$ and $J_z = \oint_{\partial V} \rho(\vec{u} \cdot \hat{n})\bar{w}\, dA$, respectively), in this case

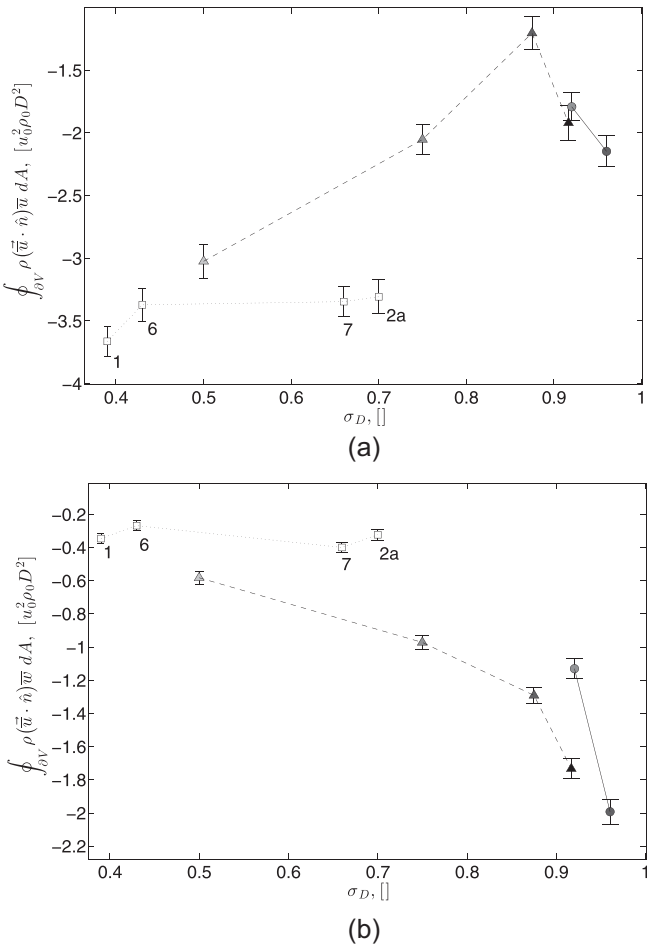

FIG. 10. (a) Streamwise and (b) vertical momentum fluxes through control volumes spanning the full fields of view in Fig. 9. □ indicates a mesh element, △ indicates a turbine element, and ○ indicates a cylinder element. Greyscale indicates rotation rate, with white being stationary and black being $\alpha = 6$. Error bars indicate the bootstrapped 95% confidence interval summed with the propagated experimental uncertainties. The lines simply connect the data points for each element type and do not represent a fitting to the data.

through control surfaces defined by the full fields of view shown in Figure 9. From these figures, it can be concluded that the meshes ($\sigma_D = [0.39, 0.43, 0.66, 0.70]$) did not induce the same J_x and J_z as the slowest rotating turbines ($\alpha = [1, 2]$, $\sigma_D = [0.5, 0.75]$), despite having overlapping ranges of σ_D. However, considering the rotating cylinders ($\alpha = [2, 4]$, $\sigma_D = [0.92, 0.96]$) and the faster rotating turbines ($\alpha = [4, 6]$, $\sigma_D = [0.88, 0.92]$), it can be seen that the range of J_x defined by the turbines encompasses the J_x as induced by the cylinders, while the range of J_z defined by the cylinders encompasses the J_z induced by the turbines. Therefore, it is suggested that a cylinder rotating at an appropriate α (between $\alpha = 2$ and 4) would induce similar mean flow behaviors to those induced by a rotating turbine operating in the range $\sigma_D \in [0.88, 0.92]$. Furthermore, across these cases, both turbine and cylinder geometries show a trend of decreasing J_x with increasing dynamic solidity and a trend of increasing J_z magnitude with increasing dynamic solidity.

In examining the complete complement of data for the cylinder and turbine geometries, the conclusions drawn from the representative data sample shown here continue to hold true: the key mean flow regions induced by the rotating turbines were also induced by the rotating cylinders, with the greatest similarities in magnitudes and spatial locations observed between moderately or rapidly rotating turbines and moderately rotating cylinders. The largest exception to this qualitative similarity was the inability of the cylinder geometry to capture certain mean velocity flow features associated with the turbine vertical structure, most notably the rotor/tower junction. Given the origin of the dissimilarity, however, these qualitative differences in mean flow patterns were largely restricted either to the very near-field of the elements or to heights lower than around the mid-height of the elements. The flow features observed for the turbines at horizontal distances important for element-element interactions and near the top edges of the elements were for the most part also observed for the cylinders.

B. Wake turbulence spectra

In addition to comparing the time-averaged flows induced by the different geometric models, it is also of interest to consider to what extent the turbulence characteristics are or are not captured. To examine this, the point-wise temporal spectra of u', v' were computed from the 6 Hz and 15 Hz data at each point in small regions of interest ($0.2D$ in the streamwise direction and $1D$ in the transverse direction) which were selected to lie in the highest turbulence intensity regions behind each turbine at streamwise positions of $x = [1, 3, 5, 7]D$. The point-wise spectra were taken and averaged over the small regions using an adaptation of Welch's method with 50% overlapping Hanning windows of length 128. Details of the analysis may be found in supplementary materials; here it is simply reiterated that the resolution of the frequency measurement for the 6 Hz data was 0.2 Hz. A representative example of the resulting v' spectra is given in Figure 11; note that variations in the individual elements led to some variations in the identifiable spectral peaks in each wake. Peak frequencies for each of streamwise position of interest for each case for the elements located at (x, y) = (0, 1) are given in Table II and similar values/trends are observed for the elements located at (x, y) = (0, 1).

There were several physical sources of (turbulent) frequencies which may be identified in the system: rotation rate harmonics, bluff-body shedding, rotating-bluff-body shedding, suppression of vortex shedding, and blade-driven dynamics. For convenience, the turbulent frequencies induced by these sources will be referred to as the different "modes" of the system. These modes may be turbulent in some or all cases.

Immediately downstream of the rotating elements, the flow is believed to be dominated by turbulence associated with the eccentric rotation of the elements.[26] Table III shows the frequency harmonics associated with the element rotation rates and the associated blade passing frequencies. These rotation-induced harmonics are indicated by normal weight, italic font in Table II.

Prior literature on single and paired cylinders has shown a progression in shedding behavior with rotation rate: a stationary cylinder will shed as a stationary bluff body; at low rotation rates, there is an increase in the shedding frequency to that of a rotating bluff body; and at higher rotation rates, there is suppression of vortex shedding.[27,28] In the case of the single

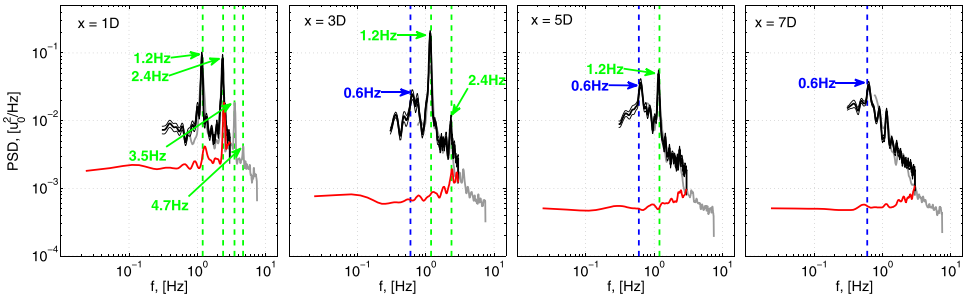

FIG. 11. Temporal spectra of v' averaged over region of interest at each indicated streamwise position for the turbine, reverse doublet, $\alpha = 1$ case. The black spectra were taken from the 6 Hz data while the gray spectra were taken from the 15 Hz data. The red shows the aliasing of the 15 Hz spectra above the 3 Hz Nyquist frequency back into the 6 Hz spectra. Dashed vertical lines indicate identified peaks, with colors as described for Table II. Thin black lines surrounding the 6 Hz spectra indicate the 95% confidence interval.

TABLE II. Frequencies of peaks in the spatially-averaged power spectral densities of v'. All values are in dimensions of Hz and the uncertainty associated with each value is ± 0.02 Hz for frequencies lower than 3 Hz and ± 0.06 Hz for frequencies higher than 3 Hz. Column headers refer to the streamwise position. Values in normal weight, italic font indicate association with rotational frequency modes. Values in bold face, upright font indicate association with stationary bluff-body shedding. Values shown in bold face, italic font indicate association with rotating bluff-body shedding. Values shown in normal weight, upright font indicate a second onset of instability in the wake. Physical drivers for the frequency followed by a "(?)" are not at present proposed.

		1D	3D	5D	7D
Turbines	$\alpha = 1$	*1.2, 2.4, 3.5,4.7*	**0.6**, *1.2, 2.4*	**0.6**, *1.2*	**0.6**
	$\alpha = 2$	*2.4, 4.8*	***0.9***, *2.4*	***0.9***	***0.9***
	$\alpha = 4$	*2.6, 4.7, 5.7*	0.5(?)	–	–
	$\alpha = 6$	*1.1*	–	–	–
Cylinders	$\alpha = 0$	**0.5**	**0.5**	**0.5**	**0.5**
	$\alpha = 2$	***0.7***, *2.4, 4.9*	***0.8***	***0.8***	***0.8***
	$\alpha = 4$	–	–	0.4	0.4

TABLE III. Association between frequencies in Hz, rotation rates, and blade passing frequencies.

Frequency (Hz)	Harmonic	Rotation rate	Blade passing frequency
1.17	First	$\alpha = 1$	–
2.34	Second	$\alpha = 2$	–
3.51	Third	–	$\alpha = 1$
4.68	Fourth	$\alpha = 4$	–
5.85	Fifth	–	–
7.02	Sixth	$\alpha = 6$	$\alpha = 2$

cylinders, it has been shown that for even further increased rotation rates there is redevelopment of shedding at a very low frequency[27] (referred to as a "second instability" in reference to the progression of increasing through α space).

These behaviors were all observed in the present data set: the stationary cylinders (in the paired configuration) exhibited a stationary-bluff body shedding frequency of $f = 0.5$ Hz (equal to a Strouhal number of 0.13, indicated by bold weight, upright font in Table II). The cylinders at $\alpha = 2$ exhibited an increased, rotating-bluff body shedding frequency of $f = 0.8$ Hz (indicated by bold weight, italicized font in Table II). The cylinders at $\alpha = 4$ exhibited vortex shedding suppression in the near field (dashes in Table II), but in the far downstream there was the appearance of a low-frequency mode $f = 0.4$ Hz, which may have been associated with the second instability (indicated by normal weight, upright font in Table II).

Prior literature on single rotating turbines has shown that the far wake of a rotating turbine has the same bluff-body shedding frequency as a stationary cylinder.[24] In the present data set, this result is also observed: the downstream turbulence behaviors of the turbines at $\alpha = 1$ was dominated by shedding at $f = 0.6$ Hz (indicated by bold weight, upright font in Table II). While this was higher than the shedding frequency observed for the paired stationary cylinders, it was in agreement with the shedding frequency found for an isolated stationary cylinder: $f = 0.6$ Hz. This suggests that while proximity-effects may alter the shedding frequency of stationary paired cylinders, slowly rotating paired turbines do not appear to be strongly effected by proximity, but effectively interact with the flow as isolated stationary bluff bodies.

The present data set further suggests an extension to the prior literature on rotating turbines: at higher rotation rates, the rotating turbines showed the same turbulence modes as rotating cylinders. In the far wake regions, the turbines at $\alpha = 2$ exhibited an increased shedding frequency over the $\alpha = 1$ value ($f = 0.9$ Hz, indicated by bold weight, italicized font in Table II) and which comes close to the rotating bluff body shedding mode of the cylinders at $\alpha = 2$. At the further increased rotation rates of $\alpha = 4$ and 6, the turbines exhibited shedding suppression in the near downstream (dashes in Table II).

To summarize, the turbines and cylinders appear to show roughly the same progression through downstream turbulence modes with increasing α: stationary bluff body (blue; bold weight, upright font), rotating bluff body (red; bold weight, italic font), and shedding suppression (dashes).

IV. DISCUSSION

Similar to prior work on rotating single and paired cylinders[27,28] and single turbines,[24] the present data suggests that the characterization of the flow around pairs of rotating turbines may be given as a progression through behaviors with increasing tip speed ratio, α, or dynamic solidity, σ_D.

For the slowest rotating turbines, $\alpha = 1$, $\sigma_D = 0.50$, the overall behavior of the flow was largely dominated by blockage effects of the turbine in that there were only relatively minor rotationally induced mean transverse and vertical flows in the immediate vicinity of the turbines, while the wake spectra showed shedding behaviors closely associated with that of a stationary bluff body. It was in this regime of turbine operation ($\sigma_D \in [0.5, 0.75]$) that the horizontal (2D cross-sectional) mean velocity flow fields were similar to those associated with porous flat plates with appropriately selected non-uniform porosity. As the porous flat plates are a model designed to capture blockage effects without any rotational effects, they are not able to capture the three-dimensional (vertical plane) mean velocity flow fields, even in this regime of dynamic solidity.

With increasing rotation rate/dynamic solidity, the turbines entered a regime in which the rotationally induced behaviors become increasingly important in comparison to the blockage effects. This was observed not only in the development and strengthening (with increasing α, σ_D) of both transverse and vertical momentum fluxes but also in the transition in wake turbulence from behaviors associated with a stationary cylinder (blockage effect only) to those associated with rotating cylinders (blockage and rotational effects). It was in this regime of behavior ($\sigma_D \in [0.88, 0.92]$) that the mean velocity flow fields were similar to those associated with moderately rotating cylinders and both geometries followed the same trends in integral mean momentum fluxes over α, σ_D.

Because the purpose of the present work was to evaluate the acceptability of lower-order turbine models for use in experimental and numerical studies of large arrays of turbines, it is worth explicitly commenting that the disagreements which do exist between the patterns of mean flow induced by the cylinders and the turbines operating within this regime were largely confined to regions very near the elements and at lower heights. The flow patterns in regions anticipated to be the most significant for interaction with other elements (i.e., horizontally removed from the element by several element diameters) and for interaction between the flow within and above the array (i.e., near the tops of the elements) were largely in qualitative agreement between the two geometries. It is again emphasized, however, that quantitative magnitude

and exact spatial locations of certain mean flow features may or may not be similar between the two geometries even when operating within similar rotation rate regimes.

For the more rapidly rotating cylinders ($\sigma_D > 0.92$), the mean flow patterns show some deviations from those associated with the turbines. Based on the observed low-frequency shedding in the far downstream of this case, it is proposed that the deviations in mean velocity patterns were associated with the re-development of flow instabilities. There was some evidence in the wake spectra that the fastest rotating turbines may also have been approaching this regime and, with further increases in α (and therefore σ_D), would have begun to show mean flow behaviors similar to the cylinders at $\alpha = 4$, but this cannot be determined exactly from the present data set.

To summarize, these results suggest that the similarities and differences between the flows around porous flat plates, rotating turbines, and rotating cylinders may be considered to lie on a continuum. In terms of laboratory and numerical experiments, the porous flat plate and actuator disk may (depending on the goals of a particular study) represent reasonable low-order models for very slowly rotating VAWT arrays, while rotating cylinders and actuator swept surfaces may (again, depending on the study goals) represent reasonable low-order models for moderately to rapidlyrotating VAWT arrays.

Relating these results back to prior experimental work on arrays of rotating cylinders,[7,8] the present work suggests that the overall patterns of the flow and the interactions both between elements and between the within-array and above-array flows would not be fundamentally changed for cylinder arrays and turbine arrays. This assumes appropriate rotation rates of each geometry such that the two geometries were operating in the same regime.

Further work is required in order to extend the present results to more general scenarios. Most importantly, the adequacy of the lower order geometric models at higher Reynolds number and for flow-driven turbines should be evaluated. Additionally, it would be of interest to further examine the dependencies of the observed turbine operational regimes on the solidity of the turbine, as has been done for the single turbine by Araya *et al.*[24] Finally, it would be highly beneficial to test at least a small array of elements of different geometries, in particular, to examine any nonlinear effects between neighboring element pairs.

SUPPLEMENTARY MATERIAL

See supplementary material for further details on the experimental method, including data collection and processing, measurement uncertainties, and determination of the flow region are included in the supplemental materials. Contour plots of the mean Reynolds stress fields are also included here interested readers.

ACKNOWLEDGMENTS

This work was supported by funding to A.E.C. from a NSF Graduate Research Fellowship and a Stanford Graduate Fellowship, by funding to J.O.D. from ONR N000141211047 and the Gordon and Betty Moore Foundation through Grant No. GBMF2645, and by funding from the Bob and Norma Street Environmental Fluid Mechanics Laboratory at Stanford University.

[1]J. O. Dabiri, "Potential order-of-magnitude enhancement of wind farm power density via counter-rotating vertical-axis wind turbine arrays," J. Renewable Sustainable Energy **3**, 043104 (2011).
[2]C. Archer, S. Xie, N. Ghaisas, and C. Meneveau, "Benefits of vertically-staggered wind turbines from theoretical analysis and large-eddy simulations," in *North American Wind Energy Academy Symposium* (2015).
[3]J. Bremseth and K. Duraisamy, "Computational analysis of vertical axis wind turbine arrays," Theor. Comput. Fluid Dyn. **30**, 387 (2016).
[4]M. Kinzel, Q. Mulligan, and J. O. Dabiri, "Energy exchange in an array of vertical axis wind turbines," J. Turbul. **13**, 1–13 (2012).
[5]M. Kinzel, D. B. Araya, and J. O. Dabiri, "Turbulence in vertical axis wind turbine canopies," Phys. Fluids **27**, 115102 (2015).
[6]D. B. Araya, A. E. Craig, M. Kinzel, and J. O. Dabiri, "Low-order modeling of wind farm aerodynamics using leaky rankine bodies," J. Renewable Sustainable Energy **6**, 063118 (2014).
[7]A. Craig, J. Dabiri, and J. Koseff, "A kinematic description of the key flow characteristics in an array of finite-height rotating cylinders," J. Fluids Eng. **138**, 070906 (2016).

[8]A. E. Craig, J. O. Dabiri, and J. R. Koseff, "Flow kinematics in variable-height rotating cylinder arrays," J. Fluids Eng. **138**(11), 11203 (2016).
[9]K. Duraisamy and V. Lakshminarayan, "Flow physics and performance of vertical axis wind turbine arrays," in *32nd AIAA Applied Aerodynamics Conference* (AIAA, 2014).
[10]S. Xie, C. Archer, N. Ghaisas, and C. Meneveau, "Benefits of collocating vertical- and horizontal-axis wind turbines in large wind farms," Wind Energy **20**, 45 (2017).
[11]D. Barsky, A. Posa, M. Rahromostaqim, M. Leftwich, and E. Balaras, "Experimental and computational wake characterization of a vertical axis wind turbine," in *32nd AIAA Applied Aerodynamics Conference* (2014).
[12]A. Posa, C. Parker, M. Leftwich, and E. Balaras, "Wake structure of a single vertical axis wind turbine," in *International Symposium on Turbulence and Shear Flow Phenomena* (2015).
[13]C. S. Ferreira, H. A. Madsen, M. Barone, B. Roscher, P. Deglaire, and I. Arduin, "Comparison of aerodynamic models for vertical axis wind turbines," J. Phys: Conf. Ser. **524**, 012125 (2014).
[14]S. Shamsoddin and F. Porte-Agel, "Large eddy simulation of vertical axis wind turbine wakes," Energies **7**, 890–912 (2014).
[15]S. Aubrun, S. Loyer, P. E. Hancock, and P. Hayden, "Wind turbine wake properties: Comparison between a non-rotating simplified wind turbine model and a rotating model," J. Wind Eng. Ind. Aerodyn. **120**, 1–8 (2013).
[16]J. Sumner, G. Espana, C. Masson, and S. Aubrun, "Evaluation of rans/actuator disk modelling of wind turbine wake flow using wind tunnel measurements," Int. J. Eng. Syst. Modell. Simul. **5**, 147–157 (2013).
[17]L. E. M. Lignarolo, D. Ragni, C. J. S. Ferreira, and G. J. W. van Bussel, "Turbulent mixing in wind turbine and actuator disc wakes: An experimental analysis," in *33rd Wind Energy Symposium* (American Institute of Aeronautics and Astronautics, 2015).
[18]R. Theunissen and C. B. Allen, "Feasibility of using porous discs for wind tunnel simulations of wind farm power variation with turbine layout," in *33rd Wind Energy Symposium* (American Institute of Aeronautics and Astronautics, 2015).
[19]D. Medici and P. H. Alfredsson, "Wind turbine near wakes and comparison to the wake behind a disc," in *43rd AIAA Aerospace Sciences Meeting and Exhibit* (American Institute of Aeronautics and Astronautics, 2005).
[20]P. Moin and K. Mahesh, "Direct numerical simulation: A tool in turbulence research," Annu. Rev. Fluid Mech. **30**, 539–578 (1998).
[21]P. R. Spalart, "Direct simulation of a turbulent boundary layer up to $r_\theta = 1410$," J. Fluid Mech. **187**, 61–98 (1988).
[22]J. Crimaldi, "Turbulence structure of velocity and scalar fields over a bed of model bivalves," Ph.D. thesis (Stanford University, 1998).
[23]D. Coles, "The law of the wake in the turbulent boundary layer," J. Fluid Mech. **1**, 191–226 (1956).
[24]D. B. Araya, T. Colonius, and J. O. Dabiri, "Transition to bluff body dynamics in the wake of vertical-axis wind turbines," J. Fluid Mech. **813**, 346–381 (2017).
[25]D. Sumner, "Flow above the free end of a surface-mounted finite-height circular cylinder: A review," J. Fluids Struct. **43**, 41–63 (2013).
[26]S. Mittal, "Flow past rotating cylinders: Effect of eccentricity," J. Appl. Mech. **68**, 543–552 (2001).
[27]S. Mittal and B. Kumar, "Flow past a rotating cylinder," J. Fluid Mech. **476**, 303–334 (2003).
[28]A. S. Chan, P. A. Dewey, A. Jameson, C. Liang, and A. J. Smits, "Vortex suppression and drag reduction in the wake of counter-rotating turbines," J. Fluid Mech. **679**, 343–382 (2011).